JOURNAL OF SPACECRAFT AND ROCKETS
Vol. 34, No. 4, July–August 1997

Navier–Stokes Computations of Finned Kinetic Energy Projectile Base Flow

Bernard J. Guidos*
U.S. Army Research Laboratory, Aberdeen Proving Ground, Maryland 21005-5066

A computational fluid dynamics (CFD) study of finned kinetic energy projectile base flow is presented for supersonic flight conditions. A parabolized Navier–Stokes technique is used to compute the attached flow over the forebody and fins. An unsteady Navier–Stokes technique is then used to compute the flow in the base region. The modeling approach and computational requirements of the problem are discussed. Base pressures from several CFD solutions at Mach numbers 3, 4, and 5 are presented, and the computed zero-yaw drag coefficients are compared with range-acquired values. Two-dimensional flow visualization of the computed base flow structure for one case is presented, indicating the extent and shape of the separated flow region. No flow axisymmetry exists in the base region, and the flow structure bears little resemblance to those of axisymmetric configurations at zero angle of attack.

Nomenclature

C_D	= total drag coefficient, (drag force)/$[\frac{1}{2}q_\infty(\pi d^2/4)]$
C_{D_B}	= base and fin trailing-edge drag coefficient
C_{D_F}	= attached flow drag coefficient
$C_{D_{\delta 2}}$	= yaw drag coefficient
C_{D_o}	= zero-yaw drag coefficient
d	= projectile reference diameter
L	= unit length
M	= Mach number
p	= pressure
q	= dynamic pressure
r	= radial coordinate
s	= arc or interval length
u, v, w	= Cartesian velocity components
x, y, z	= Cartesian coordinates; origin at nose tip x along projectile axis nose to tail
y^+	= distance from wall in boundary-layer coordinates
δ	= total angle of attack
ε	= total energy per unit volume of fluid
ρ	= density
ϕ	= roll angle

Subscripts

avg	= average value
B	= projectile base condition
wall	= wall or solid surface condition
∞	= freestream condition

Introduction

THE prediction of finned kinetic energy (KE) projectile base flow is a challenging problem in the area of applied computational fluid dynamics (CFD). The finned projectile base flowfield, even for a nonspinning configuration at 0-deg angle of attack, is a complex three-dimensional structure that demands large computer resources and innovative graphical flow visualization. Accurate modeling of the base flow will provide the base drag coefficient, an aerodynamics coefficient yet to be adequately or routinely predicted for finned KE projectiles using CFD. The flowfield details provided by CFD can impact the design of fins, base geometries, and drag-reduction or lethality enhancements such as base bleed mechanisms, rocket systems, or rear-eject submunitions.

Presented as Paper 95-3460 at the AIAA Atmospheric Flight Mechanics Conference, Baltimore, MD, Aug. 7–9, 1995; received Sept. 19, 1995; revision received April 20, 1997; accepted for publication April 25, 1997.

*Aerospace Engineer, Aerodynamics Branch. Senior Member AIAA.

In the present study, CFD solutions are generated for a finned KE projectile at Mach numbers 3, 4, and 5. Two Navier–Stokes finite difference techniques are used in conjunction. A parabolized Navier–Stokes (PNS) technique is used to compute the attached flow over the forebody and fins. An unsteady Navier–Stokes (UNS) technique is then used to compute the flow in the base region. The major objectives are 1) to characterize the computational modeling aspects of the problem, 2) to compare the total computed drag of the projectile model with range-acquired data for the actual round, and 3) to gain insight into the flowfield structure.

Projectile Configuration

The computational model of the finned projectile, illustrated in Fig. 1, is a simplified version of the actual configuration. The model possesses a conical nose section, followed by a cylindrical section of constant reference diameter d equal to 35.2 mm. The total model length is 13.94 calibers, in which 1 caliber is equal to 1 reference diameter. The small blunt nose tip of the actual model is replaced by a conical nose tip.

The six fins are equally distributed around the body and aligned with the projectile axis. The leading edges are cylindrically blunted and swept 71 deg. The trailing edges are truncated, perpendicular to the projectile axis, and aligned with the projectile base, i.e., no fin overhang. The fins are tapered from root to tip. The leading- and trailing-edge chamfers, which control the spin of the actual projectile, are omitted from the computational model. The base of the computational model is assumed to be flat, with protuberances such as the tracer cavity and the core rod/finned afterbody interface ignored.

Typical of long-rod KE projectiles, the actual projectile possesses sabot grooves over the cylindrical forebody section. These grooves act to transfer the accelerating force from the sabot, which also acts as a bore rider, to the projectile. The correlation of Mikhail[1] was used to estimate the effect of groove drag for this configuration. The correlation shows that the sabot grooves account for, at most, 1.6% of the total drag for Mach numbers between 3 and 5. With this result in hand, the grooves are replaced by a smooth surface in the computational model.

The projectile is nonaxisymmetric; therefore, a clear definition of circumferential location is essential for ensuing discussions. The roll angle of a point in the flow or on the body is defined here as the circumferential angle measured relative to one reference fin. A set of all points in space with the same roll angle is defined here as a roll plane. Roll angle and roll plane can both be denoted as ϕ without creating ambiguity. Also note that, because the angle of attack is 0 deg and the computational model has six symmetric fins, the computational flowfield is computed only between roll planes $0\,\text{deg} \le \phi \le 30\,\text{deg}$, employing symmetry principles. The $\phi = 0$ deg roll plane is coplanar with the fin plane of symmetry, whereas the $\phi = 30$ deg roll plane is located midway between two adjacent

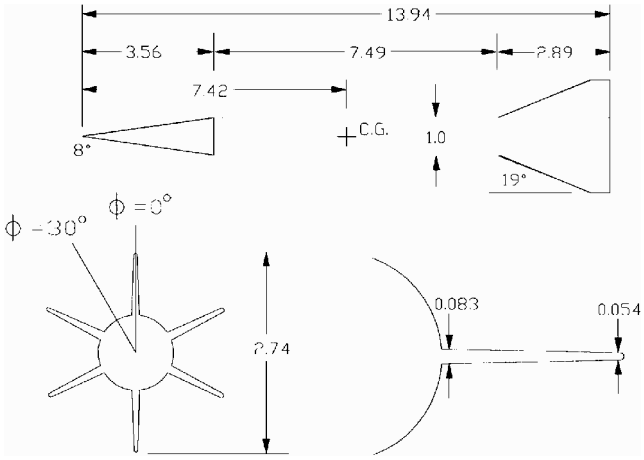

Fig. 1 Finned projectile model. All dimensions are in calibers (1 caliber = 35.2 mm).

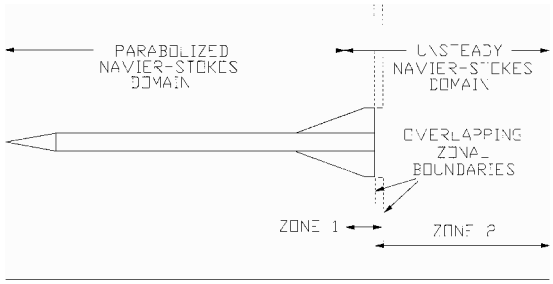

Fig. 2 Code coupling for finned projectile base flow modeling, ϕ = 0 deg.

fins. In some grid and flow visualization figures to be presented, roll plane 150 deg is used to represent roll plane 30 deg for clarity.

Flow Model for Projectile Forebody and Fins

A PNS technique is used to compute the flow over the projectile forebody and fins, as depicted in Fig. 2. The PNS code used here is a descendant of the code written by Schiff and Steger,[2] is fully implicit and approximately factored, and uses second-order central differencing following Beam and Warming.[3] In this formulation, only the thin-layer viscous terms in the outward coordinate direction are retained. The Baldwin–Lomax[4] algebraic turbulence model is used in all cases presented here. A shock-fitted outer boundary condition is used.[5] The code is used in step-back mode to generate a pointed conical nose tip solution, providing the initial conditions for downstream marching.[6] The PNS solutions for this configuration were generated using about 1–2 h of computer time per solution on a Cray X-MP computer. Details of the application of the PNS technique to this and other finned KE projectile configurations are given in Refs. 7–11.

The PNS solutions serve as the upstream inflow boundary condition for the base flow computations. The PNS solutions also provide the forebody drag contribution (from the forebody and fins), which is added to the base drag contribution (from the cylinder base and fin trailing edge) to obtain the total computed zero-yaw drag coefficient at each Mach number.

The forebody drag contribution was obtained by specifying a constant wall temperature of 294 K, which is the approximate launch temperature of the projectile through the range facility. Separate PNS solutions were generated using an adiabatic wall condition and were used to provide the inflow conditions for the ensuing base flow computations. The adiabatic wall condition was used because a full implementation of the wall temperature boundary condition did not exist at the onset of the study.

Flow Model for Projectile Base Region

Unsteady Navier–Stokes CFD Technique

The main focus of the present work is the application of a UNS technique to generate base flow solutions, also depicted in Fig. 2.

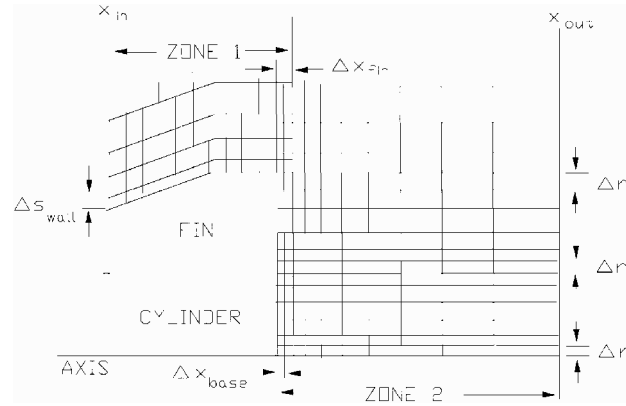

Fig. 3 Grid parameters for finned projectile base flow modeling.

The UNS approach is a time-marching approach, in which an initial assumed flowfield is integrated through time toward, in this application, a steady-state solution. The technique used here has previously been described and applied to hypersonic vehicles and is an upwind differencing code referred to as the UWIN code.[12,13] The version of the code used here is written in a two-zone grid formulation, illustrated in Fig. 3.

The governing equations are a nondimensionalized form of the time-dependent, Reynolds-averaged, thin-layer Navier–Stokes equations in three-dimensional generalized coordinates and strong conservation law form, as given by Rai.[14] The five dependent flow variables are density, three Cartesian components of momentum, and total energy per unit volume. The pressure is defined by assuming perfect gas behavior.

The governing flow equations are discretized using an approximately factored, implicit, flux-split, upwind, total variation diminishing, finite difference approach. The scheme, used here to generate steady-state solutions, is temporally first-order accurate and spatially second-order accurate. The implicit side of the discretized equation has been approximately factored following Beam and Warming.[3] The inviscid flux-split Jacobian matrices that relate the changes in the inviscid fluxes with respect to the dependent variables are given by Pulliam and Steger.[15] The viscous Jacobian matrix corresponding to the outward coordinate direction is given by Steger.[16]

The explicit terms of the discretized equation include first-order, inviscid, numerical fluxes, as well as flux differences contributing second-order spatial accuracy. These vectors, key elements of the numerical scheme, are constructed using an upwind method.[17] The flux differences are modified using a flux-limiting procedure.[18] The terms in the viscosity vector are numerically differentiated using standard second-order central differences.[14] The nonlinear form of the finite difference equations is solved by applying a Newton-iterative technique,[18] and all solutions presented here were generated using two iterations per time step.

The Baldwin–Lomax[4] turbulence model is used in the attached flow regions. Downstream from the projectile, i.e., in the base region, turbulence is not modeled, and laminar viscosity terms are retained only in the near-radial direction.

Freestream, Boundary, and Initial Conditions

Computational results are presented for freestream Mach numbers of 3, 4, and 5. The angle of attack is fixed at 0 deg, and the spin rate is fixed at 0 rpm. The freestream conditions are taken to be sea-level atmospheric values.

As already mentioned, the inflow boundary conditions for zone 1 are generated by the PNS computations that provide the flow conditions at an axial position upstream of the projectile base. The outer boundary points of zones 1 and 2 are assigned freestream values and located beyond the bow shock, which is captured within the interior of the computational domain. The downstream outflow boundary of zone 2 is specified using a first-order extrapolation of the dependent flow variables. Circumferential boundary conditions are applied in both zones by employing symmetry principles on the $\phi = 0$ and 30 deg roll planes.

Adiabatic boundary conditions are applied along all solid surface boundaries. The no-slip boundary condition is enforced, and a zero normal pressure derivative is imposed. First-order implicit boundary conditions are implemented.[14]

Zone 2 inner boundary points are assigned values depending on whether a miniature sting or an axis boundary is prescribed within the flow domain. For the cases when a miniature sting is modeled, the sting is treated as a solid, adiabatic surface. The axis boundary is handled using the following first-order boundary conditions:

$$\rho_1 = \rho_2 \qquad u_1 = u_2 \qquad v_1 = 0 \qquad w_1 = 0 \qquad p_1 = p_2 \quad (1)$$

in which the subscripts 1 and 2 refer to the axis boundary point and first interior grid point, respectively, along a radial grid line. For the three-dimensional flow situation in this study, the preceding relationships yield multivalued axis grid points. The mean values of each of these variables are calculated and used at all coincident axis points, and the total energy is then determined using the perfect gas relationship.

The zonal boundary interface, consisting of two overlapping boundaries, is located at the projectile base. Specifically, the two zonal boundaries correspond to the zone 1 outflow plane and the zone 2 inflow plane. Both zonal boundaries are perpendicular to the projectile axis and overlap each other by one or more grid points. The zone 2 zonal boundary is coplanar with the base, the fin trailing edge, and the next-to-last downstream grid plane of zone 1. The zone 1 zonal boundary is located downstream from the base and fin trailing edge and is constructed to be coplanar with either the first or one of the first upstream interior grid planes of zone 2. Because the zonal boundary is nonaligned, i.e., points do not match those of the neighboring zone, it is necessary to interpolate the values of the dependent variables within each zonal boundary plane.

An explicit, triangular, Cartesian interpolation procedure is used. The procedure is nonconservative, depending solely on the grid geometries, and so the interpolation coefficients associated with each zonal boundary point are calculated only at the onset of the computation. The interpolation procedure is not applied to those zone 2 boundary grid points that are surface points, i.e., those that constitute the projectile base or fin trailing edge. Those points are instead flagged at the onset of the computation and are updated using the adiabatic no-slip boundary procedure.

As is the case for the numerical simulation of any complex three-dimensional flowfield, the initial conditions can significantly impact the computer time needed for the solution to approach a steady state. Zone 1 initial conditions were straightforward because of the availability of the PNS solutions. Zone 2 initial conditions proved to be more sensitive because the use of freestream or outer flow initial values caused computation-ending numerical instabilities to arise in almost all cases in which they were used.

An alternate initialization procedure was implemented in an effort to stabilize the numerical solution and promote faster convergence. The zone 1 dependent variables at all axial locations were assigned values from the corresponding outward and circumferential indices of the inflow plane. The zone 2 inflow dependent variables were obtained by applying the zonal boundary interpolation scheme at all zonal boundary points, as described earlier. The cylinder base and fin trailing-edge surface grid points were assigned zero velocity, freestream total energy, and density values from the perfect gas relation. The zone 2 outflow variables were assigned freestream values. Finally, the interior grid points were assigned values by interpolating between the zone 2 inflow and outflow grid planes.

Computational Data Sets and Grids

The six CFD solutions discussed here are introduced in Table 1. All but one of the data sets were generated on a Cray X-MP/48 computer at Aberdeen Proving Ground (APG), Maryland, each using about 2 million words (2 Mw) of memory and 200 h of computing time. The most recent, and final, solution data set of the study (solution 3-B) was generated on a Cray 2 computer at APG, using about 11 Mw of memory and 1200 h of computer time. The large computational times are indicative of the exploratory nature of the study, in which computational efficiency was a secondary issue compared with the prospect of obtaining converged solutions. For instance, the TVD formulation used here was already judged to be computationally expensive on a per-time-step basis; however, it was also known to be very robust. Additional modeling considerations such as grid resolution, flowfield initialization, and the use of various subsets of viscosity terms significantly impact the convergence characteristics for this class of problem. In this sense, the single computational times shown in Table 1 may be indicative of an upper bound on the expected usage for this problem.

Table 1 Base flow computational solution data sets

Data set	M_∞	Computer	Data set size, Mb	Job size, Mw	CPU time per time step, s
3-A	3.0	Cray X-MP	10.5	1.8	21.0
3-B	3.0	Cray 2	66.0	11.3	147.0
4-A	4.0	Cray X-MP	3.6	0.6	6.0
4-B	4.0	Cray X-MP	10.5	1.8	18.0
4-C	4.0	Cray X-MP	10.5	1.8	21.0
5-A	5.0	Cray X-MP	10.5	1.8	21.0

Table 2 Grid parameters: zone 1

Data set	Grid points, axial × circ × out	x_{in}, caliber	Δx_{fin}, caliber	$\Delta s_{wall} \times 10^5$, caliber
3-A	10 × 35 × 45	13.36	0.064	5.8
3-B	30 × 35 × 45	13.36	0.00036	5.8
4-A	8 × 25 × 45	13.36	0.082	72.0
4-B	10 × 35 × 45	13.36	0.064	5.8
4-C	10 × 35 × 45	13.36	0.064	5.8
5-A	10 × 35 × 45	13.36	0.064	4.3

Table 3 Grid parameters: zone 2

Solution name	Grid points, axial × circ × out	x_{out}, caliber	Δx_{base}, caliber	Sting radius, caliber
3-A	30 × 35 × 75	17.91	0.0144	None
3-B	54 × 71 × 160	17.91	0.00036	None
4-A	24 × 25 × 45	18.77	0.082	0.00072
4-B	25 × 35 × 90	16.10	0.0144	0.00072
4-C	30 × 35 × 75	17.91	0.0144	None
5-A	30 × 35 × 75	17.91	0.0144	None

Table 4 More grid parameters: zone 2

Data set	Δr_0, caliber	Δr_1, caliber	Δr_2, caliber	No. of points across trailing edge
3-A	0.0043	0.0043	0.022	10
3-B	0.0043	0.0043	0.072	15
4-A	0.0036	none	none	2–4
4-B	0.0036	0.0022	0.022	10
4-C	0.022	0.0022	0.022	10
5-A	0.0043	0.0043	0.022	10

Tables 2–4 list the values of grid parameters used for each solution, and these parameters are illustrated in Fig. 3. Grid clustering is used in several areas and in all three coordinate directions. In any given direction, grid spacing between adjacent volume elements is limited to ±20% but is usually within ±10–15%.

Figure 4 shows the PNS and UNS grids from solution 4-C in the $\phi = 0$ and 30 deg roll planes (the latter roll plane rotated to $\phi = 150$ deg for clarity). Without exception, the gridding is composed of two-dimensional computational grid planes aligned perpendicular to the projectile axis. In zone 1, axial grid point spacing is constant except for solution 3-B, where points were clustered near the base. In zone 2, axial grid point clustering is prescribed near the projectile base, and radial grid point clustering is prescribed at three radial locations: 1) the axis (or miniature sting, when present), 2) the cylinder outer edge, and 3) the fin tip.

Figure 5 shows a cross section of the zone 1 grid of solution 3-B. Each zone 1 grid cross section is a planar elliptic grid constructed using the same approach as the PNS grids. Grid points are equally

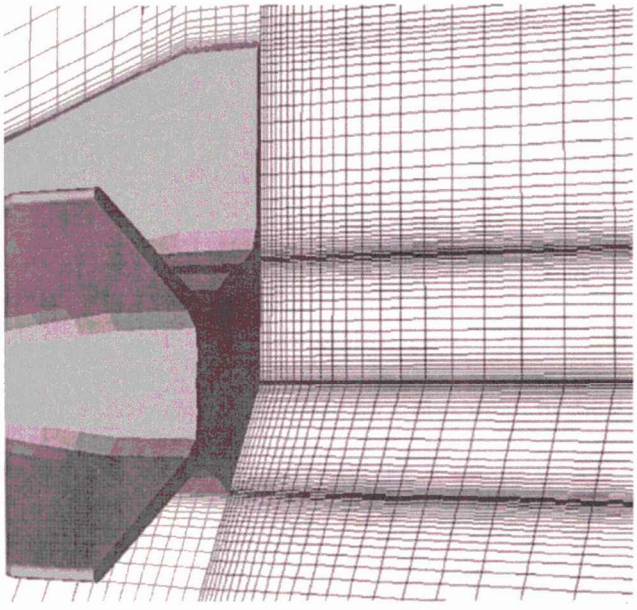

Fig. 4 Side view of grid 4-C, ϕ = 0 deg.

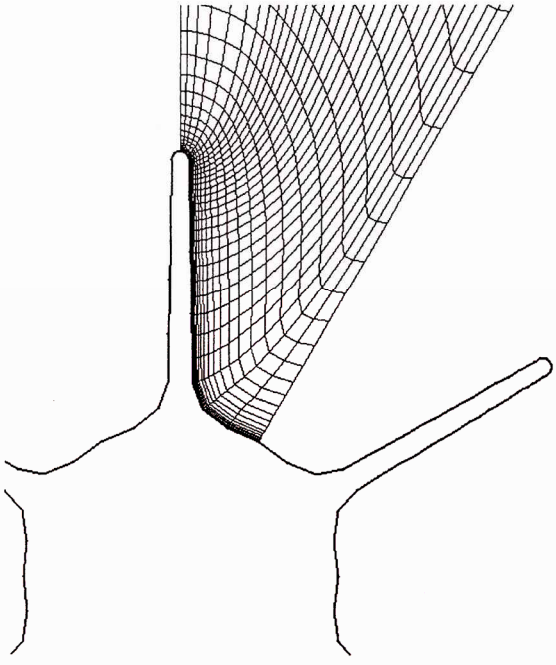

Fig. 5 Cross-sectional view of grid 3-B, zone 1, x/d = 13.94.

distributed in the axial direction, again the exception being solution 3-B, in which points are also clustered axially near the base. In all cases, grid points are radially clustered near the forebody and fin surfaces to increase the resolution of the attached boundary layer. The distance from the wall to the first interior grid point in zone 1 was determined from the PNS solutions, which used the adaptive grid procedure discussed by Sturek and Schiff.[6] The value of the boundary-layer coordinate y^+ at the first point from the cylinder and fin surface is maintained in the range from 2 to 5, although the effect of surface grid resolution on the base flow was not ascertained here.

Figure 6 shows a cross section of the zone 2 grid of solution 3-B. Each zone 2 grid cross section is algebraically constructed. The zone 2 grid is designed so that one grid line on the inflow boundary extends piecewise continuously from the axis to the outer boundary and is coincident with the fin planform edge, at least along the straight portion. Such construction aligns the grid with most of the fin planform edge, allowing gradients associated with the free shear layer formed by boundary layer separating from the trailing edge. Grid points are circumferentially clustered between this fin

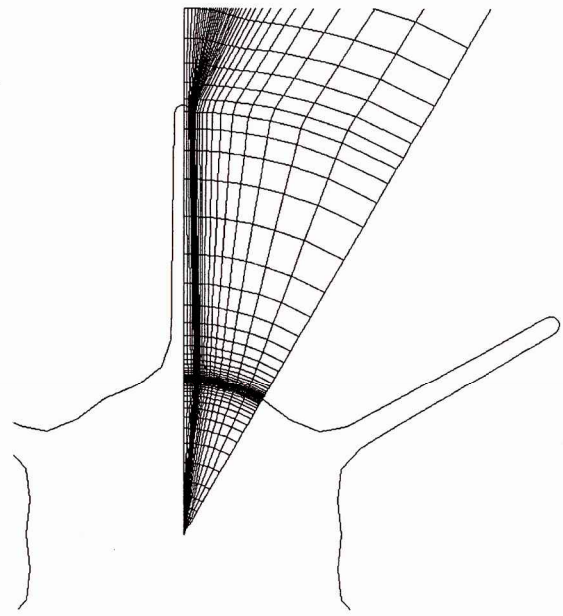

Fig. 6 Cross-sectional view of grid 3-B, zone 2, x/d = 13.94.

edge and $\phi = 30$ deg. Grid points are equally distributed across the thickness of the trailing edge, with the exception of solution 3-B, which clusters the trailing-edge points near the fin planform edge. Solutions 4-A and 4-B included a small sting in the CFD model because the axis boundary condition had yet to be implemented.

Results

Drag Comparison

The range-acquired drag coefficients were obtained from records of unpublished firings conducted at an indoor range facility at APG during 1979. The 14 shots listed here were fired with an empty tracer cavity. Spark shadowgraph data were collected within the first 200 m of flight. The total drag coefficient C_D for each shot was produced from fits of the equations of motion from Murphy.[19] The zero-yaw drag coefficient C_{D_o} was extracted from the range record of each shot for comparison to the CFD results using the relationship

$$C_D = C_{D_o} + C_{D_{\delta 2}}\delta^2 \tag{2}$$

The estimated error for C_{D_o} is $\pm 3\%$. Table 5 shows the derived values for C_{D_o} used to compare with the CFD results here.

Table 6 lists the computed zero-yaw drag coefficients and various components for the six CFD solution data sets. The computed zero-yaw drag coefficient C_{D_o} is defined as

$$C_{D_o} = C_{D_F} + C_{D_B} \tag{3}$$

in which C_{D_F} is the forebody drag contribution (which includes the forebody and fin contribution, i.e., the attached flow) obtained from the PNS code and C_{D_B} is the base drag contribution (which includes the cylinder base and fin trailing-edge drag contributions) obtained from the UNS code.

At Mach 4, the computed base drag of solution 4-A, which used the coarsest grid, is less than 60% of that of solution 4-B or 4-C, demonstrating inadequate grid resolution. In contrast, the computed base drag of solution 3-B, which used the finest grid, is only about 15% greater than that of solution 3-A, suggesting that, for the modeling assumptions used here, a grid-independent solution may be achievable using grid characteristics comparable to those of solution 3-B.

Figure 7 shows the comparison of computed and range-acquired zero-yaw drag coefficients. The UNS results from solutions 3-B, 4-C, and 5-A are combined with the PNS results (also shown) in Fig. 7. The computed drag underpredicts the range-acquired drag by about 10 and 5% at Mach 3 and 4, respectively. Because no firings were conducted above Mach 4.3, no comparison can be made for the Mach 5 case. The computed base drag is shown to compose

Table 5 Range-acquired zero-yaw drag coefficients

Shot no.	M_∞	C_{D_o}
16,405	4.30	0.300
16,423	4.29	0.301
16,404	4.28	0.306
16,424	4.26	0.303
16,421	4.24	0.307
16,422	4.22	0.306
16,416	4.12	0.308
16,417	4.11	0.307
16,401	3.87	0.326
16,402	3.87	0.329
16,403	3.76	0.343
16,419	3.45	0.373
16,418	3.44	0.370
16,420	3.02	0.412

Table 6 Computed zero-yaw drag coefficients

M_∞	C_{D_F}, PNS	Data set, UNS	C_{D_B}, UNS	C_{D_o}	(p_B/p_∞) avg
3.0	0.240	3-A	0.123	0.363	0.463
		3-B	0.143	0.383	0.376
4.0	0.222	4-A	0.047	0.269	0.636
		4-B	0.084	0.306	0.349
		4-C	0.082	0.304	0.364
5.0	0.202	5-A	0.047	0.249	0.433

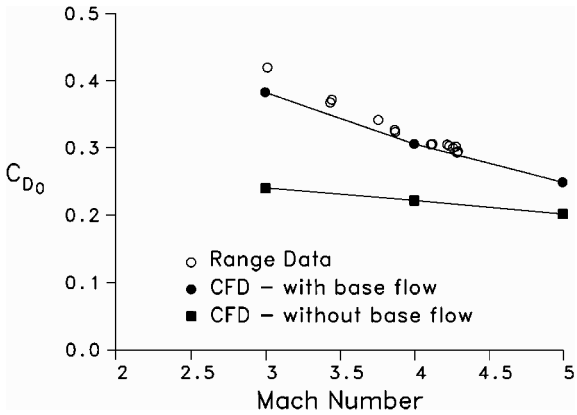

Fig. 7 Comparison of computed and range-acquired zero-yaw drag coefficients.

approximately 33, 26, and 19% of the computed total drag at Mach 3, 4, and 5, respectively.

Base Pressure

The drag comparison serves as an initial indicator of the accuracy of the CFD approach, but a more precise validation of the predicted flowfield is required because the base drag coefficient composes only a portion of the total drag. The focus of future research in this area should be the acquisition of detailed base and fin trailing-edge pressure wind-tunnel measurements for realistic configurations. The measurements reported in Refs. 20 and 21 provide additional useful validation cases. Although no further quantitative comparisons are made here, some details of the computed base flow structures are presented.

Table 6 includes the average base pressure, normalized by the freestream value for each of the six CFD solutions. The average base pressure is defined here to consist of the cylinder base and fin trailing-edge contributions. Excluding solution 4-A because of clearly inadequate grid resolution, Table 6 shows that the computed average base pressure of Mach 5 is less than that of Mach 3 but greater than that of Mach 4. Such nonmonotonic behavior of average base pressure with respect to freestream Mach number is unexpected, at least for axisymmetric base flows as well as two-dimensional trailing-edge flows. The result does not specifically eliminate the possibility that interaction between the axisymmetric-like cylinder base and two-dimensional-like trailing edge could produce such behavior but should be viewed as a possible inconsistency between solutions. The result may be attributable to inadequate grid resolution, modeling assumptions such as lack of turbulence modeling in the base region, or insufficient convergence of one or more of the CFD solutions. A conclusive interpretation cannot be made without quantitative pressure measurements with which to compare.

Figures 8–12 show the computed base pressure distributions along roll angles $\phi = 0$ and 30 deg for each of the six CFD solutions. At Mach 4, solution 4-A has much higher base pressures than solutions 4-B and 4-C, consistent with the preceding discussion of drag. Solution 4-B has a lower base pressure on the cylinder portion than solution 4-C, but the trend is reversed on the fin trailing edge, and the integrated effect leads to the similar base drag values for the two solutions, as already shown. At Mach 3, this same pressure reversal on the cylinder base and fin trailing edge is found between solutions 3-A and 3-B, although, as shown earlier, the difference in base drag is only 15%.

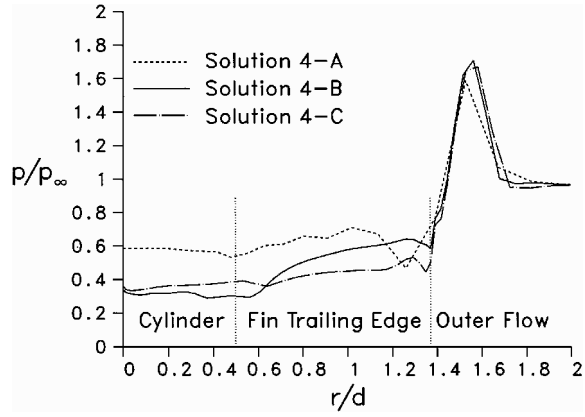

Fig. 8 Computed base pressures, $M_\infty = 4$, $\phi = 0$ deg.

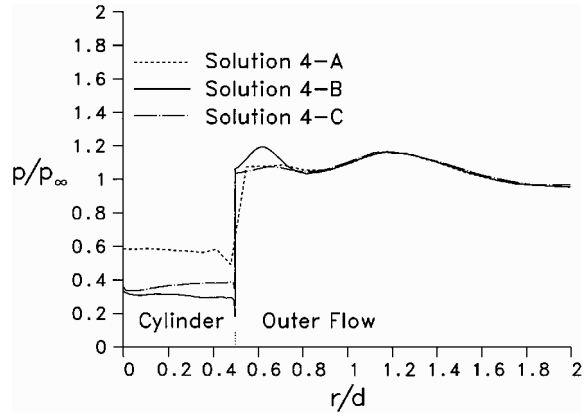

Fig. 9 Computed base pressures, $M_\infty = 4$, $\phi = 30$ deg.

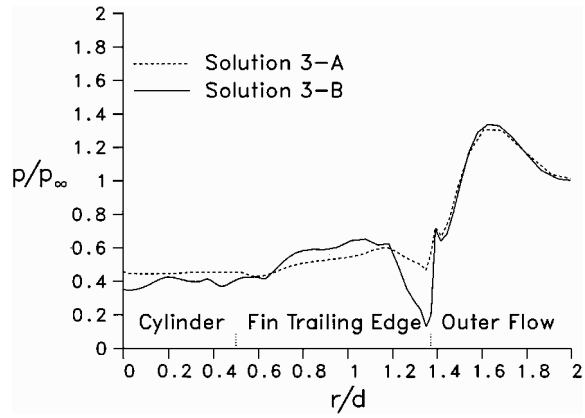

Fig. 10 Computed base pressures, $M_\infty = 3$, $\phi = 0$ deg.

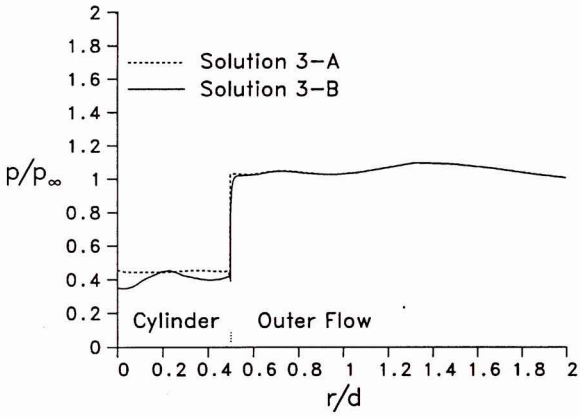

Fig. 11 Computed base pressures, $M_\infty = 3$, $\phi = 30$ deg.

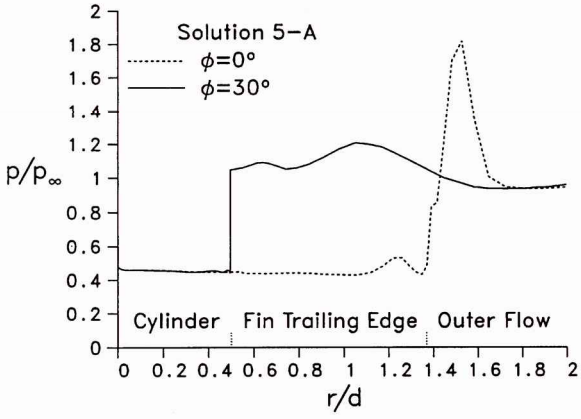

Fig. 12 Computed base pressures, $M_\infty = 5$, $\phi = 0$ and 30 deg.

All of the CFD solutions except solution 5-A show higher pressure along the fin trailing edge than on the cylinder base. Along $\phi = 30$ deg, all six CFD solutions show at least a slight undershoot in pressure near the cylinder edge, indicative of a possible need for improved grid resolution there. The same observation may apply along $\phi = 0$ deg near the fin tip. For each CFD solution, small differences between pressure distributions along $\phi = 0$ and 30 deg are apparent, but the details are inconsistent; in some cases, higher pressures exist along $\phi = 0$ deg than $\phi = 30$ deg, and in other cases the opposite is true. Of all of the pressure distributions shown here, that of solution 3-B has the most apparent saddle points, probably attributable to its finer grid resolution compared with the other five CFD solutions.

Base Flow Structure of Mach 3 Case

Figure 13 shows computed u/a_∞ contours for solution 3-B at six cross-sectional planes downstream from the base. The farthest downstream plane is approximately 1 caliber from the base. The projectile axis is plotted as a thick solid line. The light-shaded contours represent positive values, i.e., axial flow direction from nose to tail, whereas the black contours represent negative values, i.e., reverse flow. The reverse flow region depicted in each cross-sectional plane is highly nonaxisymmetric. The largest reverse flow velocity in each plane is indicated by the innermost concentric contour and represents a core flow region. In each plane, the core is located near midway between the $\phi = 0$ and 30 deg roll planes. A full cross-sectional (0 deg $\leq \phi \leq$ 360 deg) view of these contours would show 12 such core flow regions in the projectile base region. It was not strictly determined whether the reverse flow regions are in fact connected to form a single continuous reverse flow region, but no graphical or analytical indication was found otherwise. No reverse flow occurs in any cross-sectional computational plane downstream from those in Fig. 13.

Figure 14 shows another perspective of the reverse flow region in the form of negative axial velocity contours in the $\phi = 0$ and 30 deg roll planes. In the $\phi = 0$ deg roll plane, reverse flow is present only adjacent to the fin trailing edge and in a small region approximately 1 caliber downstream. The entrained particles near the fin trailing edge move primarily toward the axis before turning downstream. Adjacent to and near the cylinder base, the particles in the $\phi = 0$ deg roll plane have positive axial velocity, an indication that the particles do not enter this region from directly downstream. Figure 15 shows velocity vectors in the $\phi = 0$ and 30 deg roll planes, indicating that these particles are moving outward from the axis. It may be concluded that the particles enter this region from adjacent roll planes.

The velocity vectors in the $\phi = 30$ deg plane in Fig. 15 more closely resemble those of base flows of axisymmetric configurations at zero angle of attack. A point of familiarity is the presence of a location about which the fluid particles tend to rotate within the roll plane itself. A recognizable difference from an axisymmetric case in the $\phi = 30$ deg plane, however, is that much of the fluid near the cylinder base continues to move upstream, another indication that the particles must exit this roll plane to travel toward and feed into the $\phi = 0$ deg roll plane, as discussed earlier.

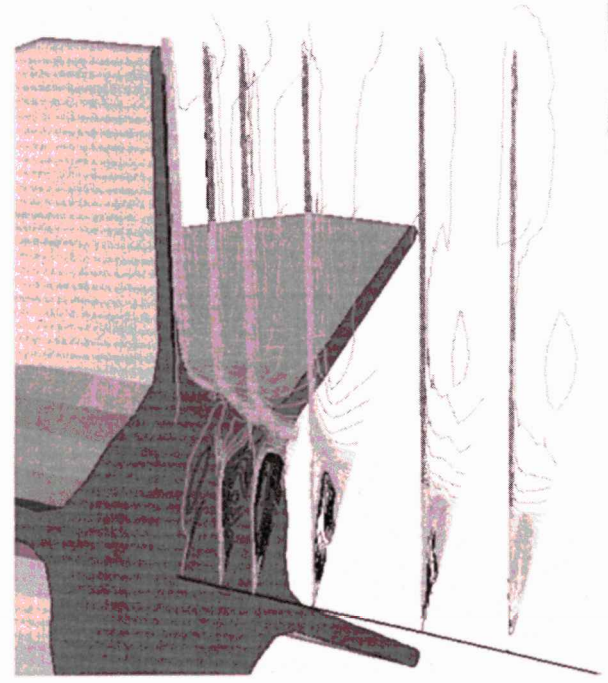

Fig. 13 Computed u/a_∞ contours (−1.4 to 4.0 in 0.2 increments), $M_\infty = 3$ (solution 3-B), at six axial locations.

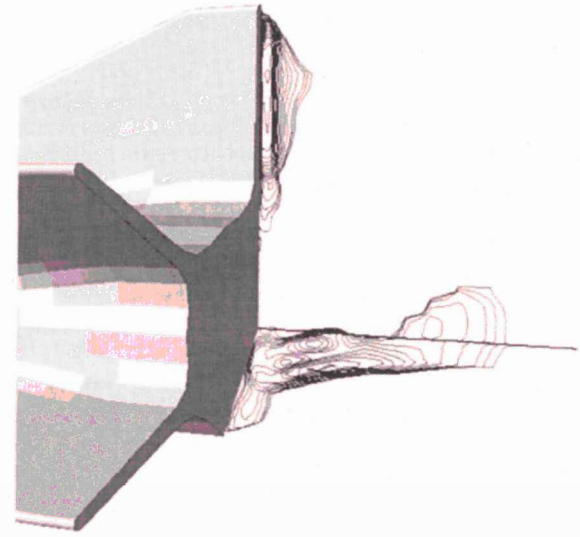

Fig. 14 Negative u/a_∞ contours, $M_\infty = 3$ (solution 3-B), $\phi = 0$ and 30 deg.

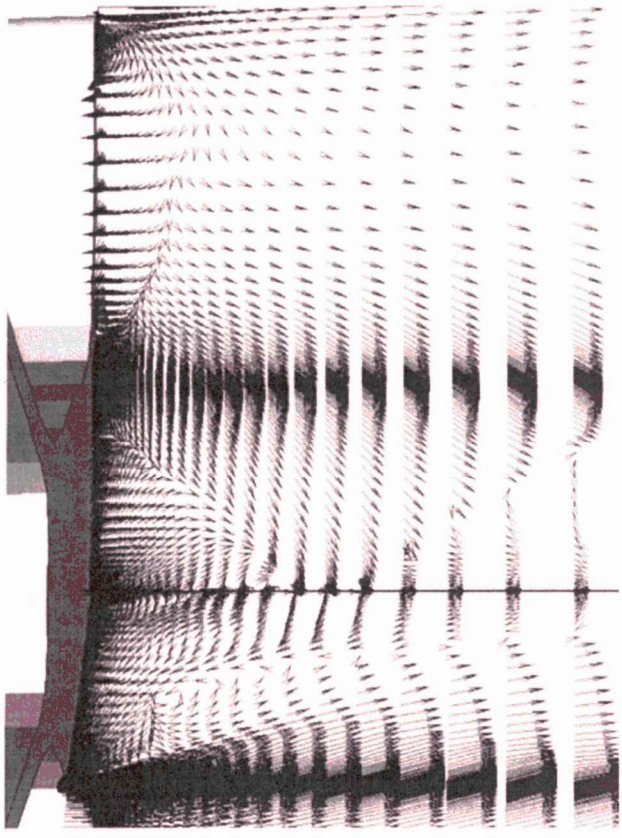

Fig. 15 Velocity vectors, $M_\infty = 3$ (solution 3-B), $\phi = 0$ and 30 deg.

Conclusion

A CFD study of finned KE projectile base flow has been presented for supersonic flight conditions. The computed zero-yaw drag of the projectile was shown to underpredict the range-acquired drag by about 10 and 5% at Mach 3 and 4, respectively. Though the drag comparison serves as an initial indicator of the accuracy of the CFD approach, it is clear that a more precise validation of finned projectile base flow CFD modeling must focus on wind-tunnel base and fin trailing-edge pressure measurements.

The two-dimensional graphical flow visualization shows that the computed base flow structure exhibits complex, fully three-dimensional features. No flow axisymmetry exists within the cylinder base region, and the flow structure is significantly different from that of an axisymmetric configuration at zero angle of attack. A major departure is that no reverse flow exists in the cylinder base region in the $\phi = 0$ deg roll plane (coincident with a fin) within $\frac{3}{4}$ caliber from the base. The region is instead fed with particles from the adjacent roll planes and from the reverse flow region adjacent to the fin trailing edge.

Many geometric, fluid mechanic, and numerical simplifications were applied in the CFD model, and a parametric determination of their individual effects on the numerical solutions needs to be fully addressed. These include such modeling aspects as geometric details, grid resolution, importance of viscosity terms, and turbulence. The task is challenging because of the large computational requirements for this class of problem. However, rapidly evolving computer architectures and facilities should make timely solutions, parametric studies, and effective visualization procedures attainable.

References

[1]Mikhail, A. G., "Drag Correlation and Predictions of Surface Groove Drag for Kinetic Energy Projectiles," *Journal of Spacecraft and Rockets*, Vol. 26, No. 5, 1989, pp. 308–313.

[2]Schiff, L. B., and Steger, J. L., "Numerical Simulation of Steady Supersonic Flow," AIAA Paper 79-0130, Jan. 1979.

[3]Beam, R., and Warming, R. F., "An Implicit Factored Scheme for the Compressible Navier–Stokes Equations," *AIAA Journal*, Vol. 16, No. 4, 1978, pp. 393–402.

[4]Baldwin, B. S., and Lomax., H., "Thin-Layer Approximation and Algebraic Model for Separated Turbulent Flows," AIAA Paper 78-0257, Jan. 1978.

[5]Rai, M. M., and Chaussee, D. S., "New Implicit Boundary Procedures: Theory and Applications," AIAA Paper 83-0123, Jan. 1983.

[6]Sturek, W. B., and Schiff, L. B., "Computations of the Magnus Effect for Slender Bodies in Supersonic Flow," U.S. Army Ballistic Research Lab., ARBRL-TR-02384, Aberdeen Proving Ground, MD, Dec. 1981.

[7]Rai, M. M., Chaussee, D. S., and Rizk, Y. M., "Calculation of Viscous Supersonic Flows over Finned Bodies," AIAA Paper 83-1667, July 1983.

[8]Weinacht, P., Guidos, B. J., Kayser, L. D., and Sturek, W. B., "PNS Computations for Spinning and Fin-Stabilized Projectiles at Supersonic Velocities," AIAA Paper 84-2118, Aug. 1984.

[9]Weinacht, P., and Sturek, W. B., "Computation of the Roll Characteristics of a Long L/D Finned Projectile and Comparison with Range Data," AIAA Paper 89-3369, Aug. 1989.

[10]Weinacht, P., and Sturek, W. B., "Navier–Stokes Predictions of Pitch Damping for Finned Projectiles Using Steady Coning Motion," AIAA Paper 90-3088, Aug. 1990.

[11]Guidos, B. J., and Weinacht, P., "Parabolized Navier–Stokes Computation of Surface Heat Transfer Characteristics for Supersonic and Hypersonic KE Projectiles," U.S. Army Research Lab., ARL-TR-191, Aberdeen Proving Ground, MD, Aug. 1993.

[12]Edwards, T., Chaussee, D., Lawrence, S., and Rizk, Y., "Comparisons of Four CFD Codes as Applied to a Hypersonic All-Body Vehicle," AIAA Paper 87-2642, Aug. 1987.

[13]Edwards, T. A., "The Effect of Exhaust Plume/Afterbody Interaction on Installed Scramjet Performance," NASA TM 101033, Dec. 1988.

[14]Rai, M. M., "Three-Dimensional Navier–Stokes Simulations of Turbine Rotor-Stator Interaction; Part I—Methodology," *Journal of Propulsion and Power*, Vol. 5, No. 3, 1989, pp. 305–311.

[15]Pulliam, T. H., and Steger, J. L., "On Implicit Finite-Difference Simulations of Three-Dimensional Flow," AIAA Paper 78-0010, Jan. 1978.

[16]Steger, J. L., "Implicit Finite-Difference Simulation of Flow About Two-Dimensional Bodies," *AIAA Journal*, Vol. 16, No. 7, 1978, pp. 679–686.

[17]Chakravarthy, S. R., and Osher, S., "High Resolution Applications of the Osher Upwind Scheme for the Euler Equations," AIAA Paper 83-39390, July 1983.

[18]Rai, M. M., and Chakravarthy, S. R., "An Implicit Form for the Osher Upwind Scheme," *AIAA Journal*, Vol. 24, No. 5, 1986, pp. 735–743.

[19]Murphy, C. H., "Free Flight Motion of Symmetric Missiles," Ballistic Research Labs., Rept. 1216, Aberdeen Proving Ground, MD, July 1963.

[20]Berner, C., Demeautis, C., and Duffner, P., "Vol de deux projectiles separes par une faible distance. I.1: Visualisation des ecoulements et mesures de pression autour de projectiles de reference," Institut Franco-Allemand de Recherches de Saint-Louis, Rapport R 107/92, France, May 1992.

[21]Moore, F. G., and Hymer, T., "Base Drag Prediction on Missile Configurations," AIAA Paper 93-3629, Aug. 1993.

R. M. Cummings
Associate Editor